AIP | Journal of Renewable and Sustainable Energy

Evaluation of the lifting line vortex model approximation for estimating the local blade flow fields in horizontal-axis wind turbines

T. Sant, V. del Campo, D. Micallef, and C. S. Ferreira

Citation: Journal of Renewable and Sustainable Energy **8**, 023302 (2016); doi: 10.1063/1.4942785
View online: http://dx.doi.org/10.1063/1.4942785
View Table of Contents: http://scitation.aip.org/content/aip/journal/jrse/8/2?ver=pdfcov
Published by the AIP Publishing

Evaluation of the lifting line vortex model approximation for estimating the local blade flow fields in horizontal-axis wind turbines

T. Sant,[1,a)] V. del Campo,[2] D. Micallef,[1,3] and C. S. Ferreira[4]
[1]*Department of Mechanical Engineering, Faculty of Engineering, University of Malta, Msida, Malta*
[2]*ETSEIAT, Universitat Politècnica de Catalunya, Terrassa, Spain*
[3]*Department of Environmental Design, Faculty of the Built Environment, University of Malta, Msida, Malta*
[4]*DUWIND, Faculty of Aerospace Engineering, Delft University of Technology, Delft, The Netherlands*

(Received 8 August 2015; accepted 12 February 2016; published online 1 March 2016)

Lifting line vortex models have been widely used to predict flow fields around wind turbine rotors. Such models are known to be deficient in modelling flow fields close to the blades due to the assumption that blade vorticity is concentrated on a line and consequently the influences of blade geometry are not well captured. The present study thoroughly assessed the errors arising from this approximation by prescribing the bound circulation as a boundary condition on the flow using a lifting line free-wake vortex approach. The bound circulation prescribed to free-wake vortex model was calculated from two independent sources using (1) experimental results from SPIV and (2) data generated from a 3D panel free-wake vortex approach, where the blade geometry is fully modelled. The axial and tangential flow fields around the blades from the lifting line vortex model were then compared with those directly produced by SPIV and the 3D panel model. The comparison was carried out for different radial locations across the blade span. The study revealed the cumulative probability error distributions in lifting line model estimations for the local aerofoil flow field under both 3D rotating and 2D non-rotating conditions. It was found that the errors in a 3D rotating environment are considerably larger than those for a wing of infinite span in 2D flow. Finally, a method based on the Cassini ovals theory is presented for defining regions around rotating blades for which the lifting line model is unreliable for estimating the flow fields.
 [http://dx.doi.org/10.1063/1.4942785]

NOMENCLATURE

a	Distance of focal point of Cassini oval from origin (m)
b	Cassini oval parameter (m)
c	Local blade chord (m)
F_a	Cumulative probability in axial flow velocity error (%)
F_t	Cumulative probability in tangential flow velocity error (%)
N	Total number of data points in flow domain (-)
n_a	Number of data points with an error in the axial flow velocity not exceeding a given value
n_t	Number of data points with an error in the tangential flow velocity not exceeding a given value

[a)]Author to whom correspondence should be addressed. Electronic mail: tonio.sant@um.edu.mt

p Maximum radius of "*no-go*" region around blade section (m)
P Probability (%)
q Minimum radius of "*no-go*" region around blade section (m)
r Radial location along blade span (m)
R Rotor tip radius (-)
$\bar{r}$ Dimensionless radial location at vortex core (-)
r_c Vortex filament core radius (m)
r_0 Initial vortex core radius (m)
Re Reynolds number (-)
Re_v Vortex Reynolds number (-)
t Time (s)
t_0 Initial time (s)
t_1 Distance perpendicular from rotor plane defining outer boundary of flow domain (m)
t_2 Distance perpendicular from rotor plane defining inner boundary of flow domain (m)
U_∞ Free wind speed (m/s)
V_a Axial flow velocity aligned with rotor axis (m/s)
V_r Relative flow velocity (m/s)
V_t Tangential flow velocity (m/s)
V_θ Tangential velocity of vortex filament
α Angle of attack (deg)
α_L Empirical constant in vortex core growth model
β Local blade pitch angle (deg)
Γ Circulation of wake filament (m^2/s)
Γ_B Blade bound circulation (m^2/s)
δ_v Turbulent viscosity coefficient
ϵ Vortex filament strain
$\varepsilon_{i,a}$ Error normalised with respect to free wind speed (m/s)
$\varepsilon_{\max}$ Maximum acceptable error for which cumulative probability error is computed (%)
λ Rotor tip speed ratio (-)
μ Strength (m/s)
ϕ Local inflow angle (deg)
Ω Rotor angular speed (rad/s)

I. INTRODUCTION

Aerodynamics plays a fundamental role in the conversion of the kinetic energy in the wind into mechanical energy. Having a better understanding of the various aerodynamics processes is essential for reliable prediction of the energy yield, rotor dynamic loads, noise generation, and wake evolution. A thorough review of the state of the art knowledge and the progress in wind turbine aerodynamics may be found in Refs. 1–5. Since the character of the Navier-Stokes equations is such that their Direct Numerical Simulation (DNS) is unfeasible for practical purposes, other numerical approaches have been developed in order to obtain the flow field around and behind the rotor. On the one hand, the Blade-Element-Momentum Theory (BEMT) approach, in which the rotor is modelled as an actuator disc, is still the most common method for engineering design applications. The method, though being very computationally efficient, lacks the physics necessary to capture certain rotor aerodynamic phenomena with a sufficient level of detail. On other hand, solving the Navier-Stokes equations with simplifying assumptions such as Reynolds Averaging (RANS) is more physically comprehensive, but its implementation is still too computationally expensive to be fully integrated in design codes involving multi-disciplinary modelling. Vortex wake methods offer a compromise between the above mentioned methods. In these numerical approaches, the flow is assumed to be incompressible and inviscid, while vorticity formed around the blades is modelled to convect into the wake as trailing and shed vorticity. The local velocity at different points in the flow field is assumed to be equal to the sum of the free stream velocity and that induced by all vorticity sources (from

the wake and blades). The circulation in the wake is represented by a series of vortex filaments that can take the form of lines[6–8] or particles.[9,10] Circulation around the blades is modelled with a lifting line or a lifting surface. Panel methods apply the same approach for modelling the wake, but the blade geometry is taken into account more accurately by distributing vorticity sources along the blade profile.[11,12] Viscous effects can be included by integrating a boundary layer model. Consequently, panel methods are computationally more demanding than the lifting line approximation. The latter is however more convenient for routine engineering design computations given that it allows for direct use of aerofoil lift and drag data and engineering models to account for stall delay[13] and dynamic stall phenomena.[14] Unlike the simple BEMT approach, free-wake vortex methods offer the capability of computing the flow velocities at any desired point. Despite significant progress in wind turbine aerodynamics research, literature sources documenting free-wake lifting line model errors when estimating the flow field around wind turbine blades are still fairly limited.

The present study assesses the capability of the lifting line approach integrated with a free-wake vortex model in simulating the axial and tangential flow fields in the close proximity of horizontal-axis wind turbine (HAWT) blades. It aims at providing a better understanding of the extent to which reliable estimates for the flow field can be derived from lifting line free-wake vortex models. The discrepancies between the flow field predictions in the central parts of the blade, where the flow had a more 2D nature, and the outer part of the blades, where 3D flow phenomena become more dominant, will also be discussed. This paper is organised as follows: The methodology and the rotor geometry used will be described first. A brief description of the experimental techniques (Stereo Particle Image Velocimetry, SPIV) and the numerical models (Panel Vortex and Lifting Line with Free Vortex Wake) used in this study is then presented. Finally, the results obtained will be presented and discussed. The Cassini ovals theory is employed in conjunction with the SPIV measurement data to establish "*no-go*" regions around which could serve as a guideline when estimating flow fields around the wind turbine rotor blades using a lifting line free-wake vortex method.

II. METHODOLOGY

A. General approach

The study analyzed the axial (V_a) and tangential (V_t) flow velocity components in the close vicinity of the wind turbine blades, with the rotor operating at a fixed tip speed ratio $\lambda = 7$. Such conditions yielded low angles of attack over the entire blade. The flow around the blades could therefore be assumed to be fully attached. The flow field at six different planes located at r/R equal to 0.4, 0.55, 0.7, 0.82, 0.9, and 0.96 was considered, with each plane aligned with local blade cross section. The following independent experimental data and numerical models were used to obtain V_a and V_t *at* each of these six reference planes:

(a) SPIV experimental measurements.
(b) 3D vortex Panel model (PM).
(c) Lifting Line Free-Wake Vortex model (LLM), with a prescribed bound circulation distribution $\Gamma_B(r)$ estimated directly from the SPIV measurements using the method adopted by del Campo *et al.*[15] The latter involved a 3D formulation to estimate the blade pressure distributions and aerodynamic loads from the measured flow velocity field.
(d) LLM with a prescribed bound circulation distribution $\Gamma_B(r)$ derived from the PM computations.

Figure 1 summarises the main procedure adopted in this study for the rotor in question. The flow field comparisons for V_a and V_t, included: (l) panel model versus SPIV (*PM-PIV);* (2) lifting line model versus SPIV (*LLM-PIV*); and (3) lifting line model versus panel model (*LLM-PM*). Finally, flow field comparisons between the lifting line model and the panel method (*LLM-PM*) are carried out for equivalent 2D flow (non-rotating) conditions for a wing of infinite span. In this way, it could be established whether discrepancies between the lifting line and panel models for the flow field around a rotating blade are larger than those obtained under a

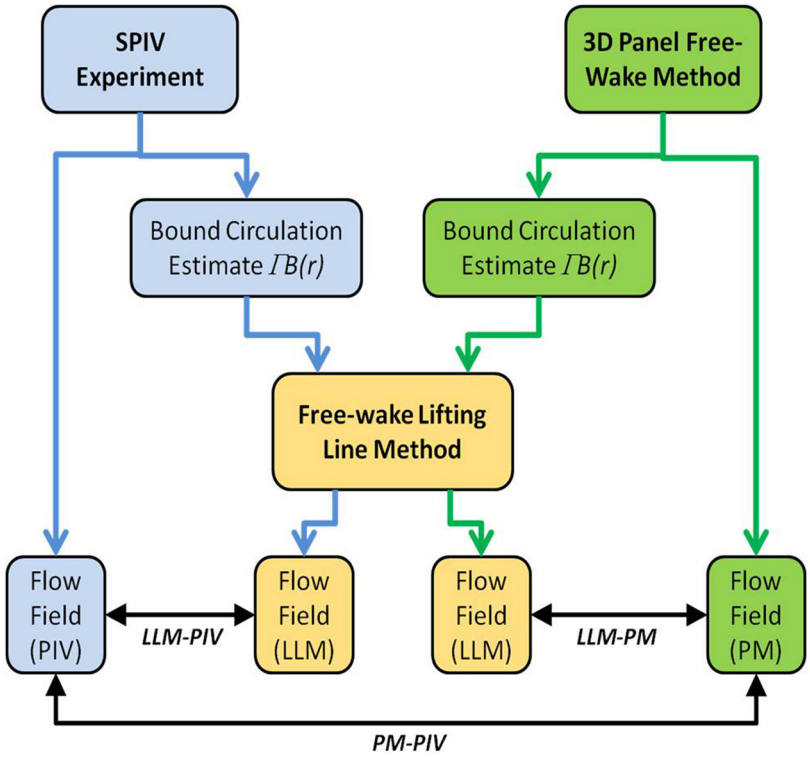

FIG. 1. Organisation of work for comparing local flow fields for rotating the wind turbine blade.

purely 2D flow environment. In the lifting line modelling for both rotating and non-rotating cases, the bound circulation was modelled as a lumped vortex concentrated at the quarter chord location.

B. TUDelft rotor geometry

The tested HAWT model at TUDelft had a rotor diameter equal to 2 m. The two-bladed rotor was coupled to an electrical drive that rotated it at a constant angular velocity. The blade sections had the geometric profile of a DU-96-W180 aerofoil for the span locations $0.147 \leq r/R \leq 1$. The innermost locations in the proximity of the hub had a circular cross-section. The blade was tapered and twisted, as can be seen in Figure 2. The blade tip had a rectangular tip with a thickness of around 2 cm.

C. Wind tunnel measurements

The experimental campaign presented herein was performed at the Open Jet Facility (OJF) at TUDelft. The closed circuit wind tunnel has an octagonal jet exit equivalent to a 3 m diameter and the size of the test section is 6 m × 6.5 m × 13.5 m. The flow velocity was fixed to 6 m/s. The rotor speed was maintained constant at 400 rpm, resulting in a Reynolds number of about 300 000 at the blade tip. The HAWT model was tested in axial conditions, as shown in Figure 3. A blade tip pitch setting equal to 0° was used. 100 SPIV images were obtained for each phase-locked velocity plane. Two cameras and the laser were mounted in a computerized traverse system. Table I presents main SPIV imaging and acquisition parameters. The flow field domain at each plane was rectangular positioned to encompass the entire blade section and with the longer sides aligned parallel to the rotor plane. Mean bound vorticity was calculated from each SPIV plane considered, using 10 different rectangular paths surrounding the blade. Further details on the experiment can be found in Refs. 15 and 16.

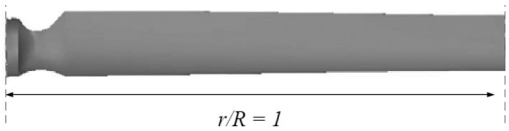

(a) blade planform

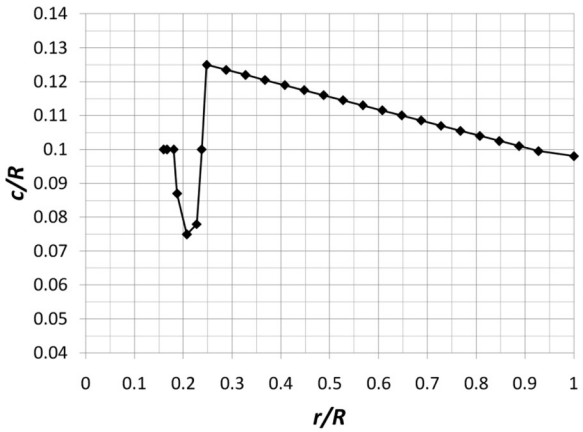

(b) chord distribution

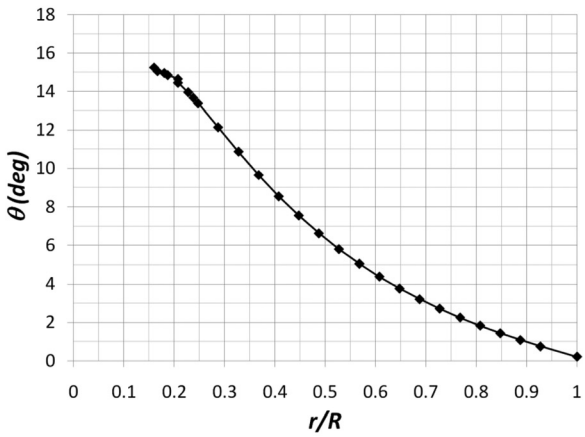

(c) twist distribution

FIG. 2. Blade geometry of the tested rotor.

Errors in the SPIV measurements were caused by cross-correlation uncertainty and peak locking. Cross-correlation errors arise from the process of computing the position of the correlation peak with sub pixel accuracy; a typical value of $\varepsilon_{cc} = 0.05 - 0.1$ pixel standard error is associated with a three-point Gaussian peak fit estimator using uniform weight kernels (see Westerweel *et al.*[17]). Due to statistical convergence, the effect of this uncertainty decreases with the square root of the number of samples (here $N = 100$), resulting in a velocity error of less than 0.1 m/s (2% of the free tunnel velocity $V_\infty = 6$ m/s).

Peak locking consists of an improper sub-pixel displacement estimation that tends to bias the results to integer values (see Rafal *et al.*[18]). The error due to peak locking was assessed by a statistical analysis on the displacement histograms, plotting the difference between the estimated shifts and their rounded offvalues. The result brought up a bias displacement error of $\varepsilon_{pl} = 0.02$px, which led to an uncertainty in velocity of less than 0.2 m/s. The two uncertainties sources in the SPIV measurements are summarised in Table II. Both are noted to be small as compared to the free-stream velocity.

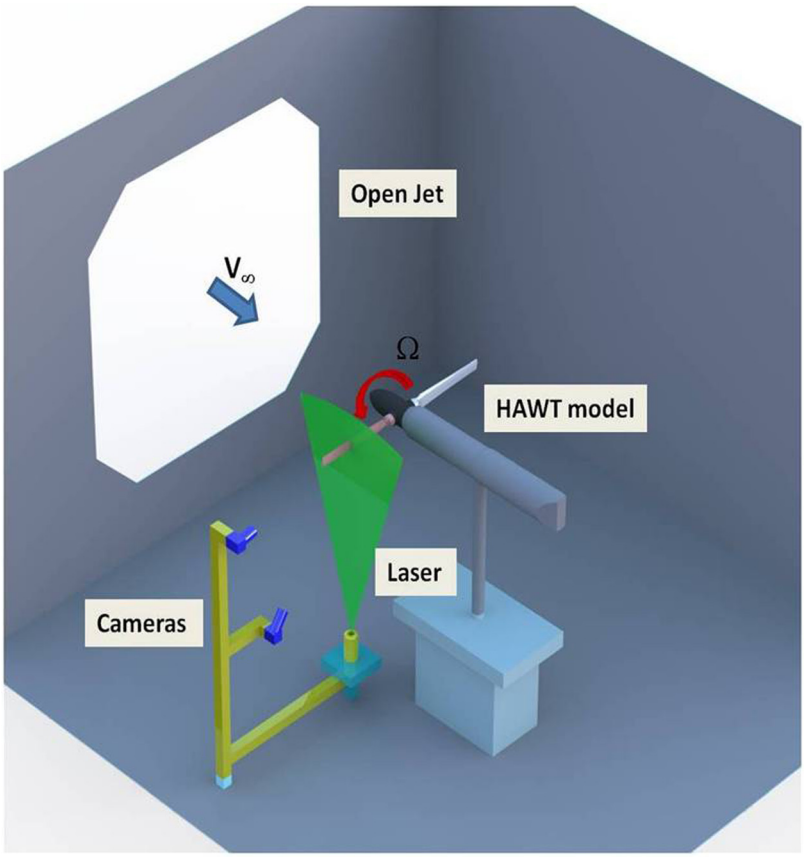

FIG. 3. SPIV experimental set up.

TABLE I. SPIV imaging and acquisition parameters.

Laser type	NdYAG (300 mJ)
Seeding	Diethylene glycol and water
Camera resolution	$4830 \times 3230\ \text{px}^2$
Field of view	$230 \times 210\ \text{mm}^2$
Spatial resolution	1.8 mm
Interrogation window	32×32 (50% overlap)

D. Free-wake vortex panel method

The PM used is a 3D unsteady potential flow model and can solve multi-body, unsteady problems. The blades are modeled with 3D surface panels of sources and doublets with a constant distribution. The doublets are shed into the wake from the trailing edge at every time step. The non-entry requirement on the airfoil surface is implemented by imposing a Dirichlet

TABLE II. Uncertainties in the SPIV flow velocity measurements.

Uncertainties	Reference	Velocity	Velocity Ratio
Cross-correlation	$\varepsilon_{cc} = 0.1\text{px}$	$\Delta V \leq 0.1\text{m/s}$	$\Delta V/V_\infty \leq 0.02$
Peak locking	$\varepsilon_{\text{pl}} = 0.02\text{px}$	$\Delta V \leq 0.2\,\text{m/s}$	$\Delta V/V_\infty \leq 0.035$

boundary condition on the potential function. The vorticity at the trailing edge is set equal to zero to satisfy the Kutta condition. Therefore, the near wake doublet strength is given by the difference in doublet strengths between upper and lower surfaces of the airfoil

$$\mu_{wt} = (\mu_u - \mu_l)_t, \tag{1}$$

where μ represents the strength of each doublet, W denotes the wake while u, l, and t refer to the upper surface, lower surface, and time, respectively. The motion of the bodies is represented by the following relation:

$$\frac{\partial \Phi}{\partial n} = \left(\vec{U_\infty} + \vec{V_{rel}} + \vec{\Omega} \times \vec{r}\right).\vec{n} \tag{2}$$

where Φ is the velocity potential, $\vec{n}$ is a unit vector normal to a given surface, $\vec{r}$ is the position coordinate along the body. The Biot-Savart law is used to compute the induced velocity from the vorticity sources at each vertex interconnecting the wake filaments. A first order Euler time-marching scheme is used to update the position of each wake vertex after every incremental time step. The latter is determined by the rotor azimuthal increment prescribed by the code user. A cosine distribution is applied for the spanwise and chordwise distribution of the blade panels. The panel method is also used to model the presence of the nacelle. Since the nacelle is a bluff body, its wake cannot be simply modelled as a thin vorticity sheet. Therefore, the wake developed by the nacelle is ignored in the model. Wake viscous effects are modelled through the application of vortex core and vortex core growth models applied on all wake vortex filaments. The following vortex core model proposed by Ramasamy and Leishman[19] is implemented:

$$V_\theta = \frac{\Gamma}{2\pi r}\left[1 - \sum\nolimits_{n=1}^{3} a_n e^{-b_n \bar{r}^2}\right]. \tag{3}$$

In the above equation, V_θ is the tangential velocity generated by the vortex having a circulation strength Γ. a_n and b_n are curve fitting parameters obtained from Ref. 20, while $\bar{r}$ is dimensionless core radius, normalised with respect to the core size. The vortex core growth model is used to model the increase in the radius of the wake filaments as they are shed from the trailing edge of each blade[18]

$$r_c = \sqrt{r_0^2 + 4\alpha_L v(1 + a_1 \mathrm{Re}_v)t}, \tag{4}$$

where r_c is the vortex core radius; r_0 is the initial core radius; α_L is the empirical constant equal to 1.25643; a_1 is the empirical constant equal to 6.5×10^{-5}; and t is the wake age. The vortex Reynolds number, Re_v, is the ratio of the vortex circulation strength and v is the kinematic viscosity. The value for r_0 is found through

$$r_0 = \sqrt{4\delta_v \alpha_L v t_0}, \tag{5a}$$

where δ_v = turbulent viscosity coefficient; and t_0 = initial time. The influence of filament stretching on the core size of the individual filaments is also modeled using the following equation:

$$r_c = r_{c,0}\left(\frac{1}{\sqrt{1+\epsilon}}\right), \tag{5b}$$

where $r_{c,o}$ is the core radius without straining and ϵ is the filament strain. Finally, the far wake is modelled by a number of vortex rings. More information about the vortex PM can be found in Refs. 15, 16, 21, and 22.

E. Lifting line free-wake vortex model

The LLM was developed by Sant *et al.*[23] The code generates an inflow distribution across any defined plane from a known bound circulation distribution prescribed by the user at the rotor blades. Each blade is modeled using lifting line piecewise elements at the quarter chord location, with their width decreasing gradually towards the blade tip and root in accordance with a cosine distribution. The near wake is modeled using a vortex sheet per blade, each consisting of a mesh of filaments to account for trailing vorticity shed by the rotating blades. Viscous effects in the near wake are accounted for through the same vortex core, core growth, and filament stretching models implemented in the panel vortex model described in Section D. A far wake model is also included and consists of a single prescribed helix per blade to approximate a fully rolled up tip vortex.

III. RESULTS AND DISCUSSION

A. Bound circulation distributions

Figure 4 plots the radial distributions of the two bound circulation distributions that were obtained independently from the panel code (PM) and SPIV measurements. The bound circulation from the panel method is computed as part of the solution process. For the experiment, the bound circulation is obtained by integrating the velocity field over a rectangular path using the method applied by del Campo *et al.*[15] It is derived using 100 different rectangular paths around the aerofoil for each radial position where SPIV data was available. The different paths were noted to produce very small discrepancies in the circulation. The standard deviation for the derived bound circulation at each radial location was found not to exceed 0.3% of the corresponding mean value.

There are notable differences between the two distributions plotted in Fig. 4. These are primarily due to the following reasons:

- The relatively low Reynolds number (125 000–300 000) along the blades suggests that viscous effects were more dominant than in the case of full-scale wind turbines. While such effects are accounted for in the derivation of the bound circulation from the SPIV measurements, there are not taken into consideration in the panel model. The latter model is only based on an inviscid formulation and no correction for the presence of a viscous boundary layer forming at the blades' surfaces is implemented. Consequently, the panel method predicts a high lift force, hence also a higher circulation, for $0.3 < r/R < 0.9$ than what would otherwise be obtained if

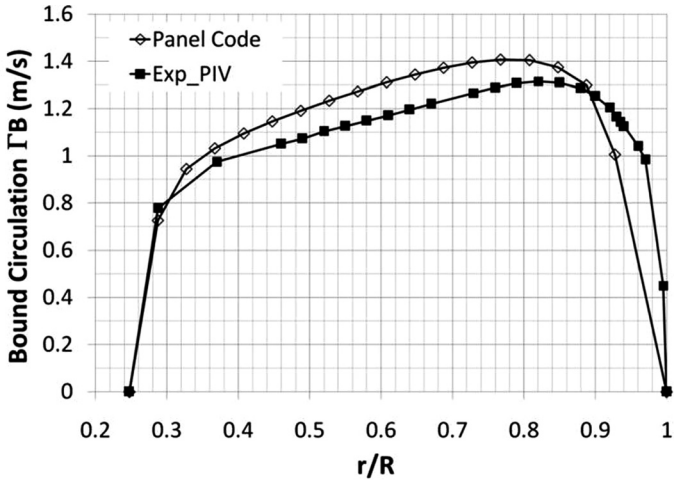

FIG. 4. Bound circulation distributions obtained independently for the TUDelft rotor using the panel code and SPIV measurements.

TABLE III. Velocity relative errors.

Axial flow	Tangential flow
$\varepsilon_{1,a} = \frac{V_{a,PM} - V_{a,PIV}}{U_\infty}$	$\varepsilon_{1,t} = \frac{V_{t,PM} - V_{t,PIV}}{U_\infty}$
$\varepsilon_{2,a} = \frac{V_{a,LLM} - V_{a,PM}}{U_\infty}$	$\varepsilon_{2,a} = \frac{V_{t,LLM} - V_{t,PIV}}{U_\infty}$
$\varepsilon_{3,a} = \frac{V_{a,LLM} - V_{a,PIV}}{U_\infty}$	$\varepsilon_{3,t} = \frac{V_{t,LLM} - V_{t,PIV}}{U_\infty}$

viscous effects are included in the simulations. These observations are corroborated by the earlier findings of del Campo *et al.*[15] where the same panel code over-predicted the normal force loading distribution along the blades as compared to that derived using the combined application of the 3D momentum equation and SPIV measurements.

- The panel code underestimates the bound circulation in the tip region ($r/R > 0.9$). This is mainly because no bound vorticity is modeled in the panel code on the flat blade tip face.[24] This effect of this limitation is more evident in the present model rotor given the large chord and finite thickness of the blade tip (see Fig. 2(a)). They are however expected to be less significant in full-scale wind turbine blades due to a larger aspect ratio and a gradually decreasing chord at the tip.

B. Error analysis for the flow field predictions by the wind turbine lifting line model

A 2D grid linear interpolation was applied within the six radial planes ($r/R = 0.4$, 0.55, 0.7, 0.82, 0.9, and 0.96) to all numerical predictions to estimate the flow velocities at the grid nodes for which the SPIV measurements were available. In order to assess quantitatively the capability of lifting line free-wake vortex method in modelling, the flow around rotating wind turbine blades, relative errors were computed at each grid node as indicated in Table III, where U_∞ is the free stream velocity.

It should be pointed out that the error computations were performed for the two independent cases in which the bound circulation (hence the blade lift) distribution of the lifting line model is equal to that of the panel code and measurements, respectively (see Figure 1). The error computations were not conducted in the close vicinity of the blade's surface given the technical constraints of the adopted SPIV measurement technique.

Figure 5 presents the contour plots for the errors $\varepsilon_{2,a}$ and $\varepsilon_{3,a}$ in the axial flow velocities (V_a). Figures 5(a)–5(c) present the differences between the LLM predictions at r/R equal to 0.4, 0.7, and 0.96 and those from the PM. Figures 5(d) and 5(e) show the differences between the LLM predictions and the SPIV measurements. As expected, the relative error is largest close to the blades, decreasing to lower than 10% further away from the aerofoil. Comparing Figures 5(a)–5(c) with Figs. 5(d)–5(f), one can note a relatively good agreement between the spatial distribution of the relative error based on the panel code prediction ($\varepsilon_{2,a}$) and the SPIV measurements ($\varepsilon_{3,a}$). It is possible to clearly identify from Figure 5 the regions around the blades at which the lifting line free-wake model is capable of modelling the axial component of the flow reliably in a complex 3D rotating environment. These regions are mainly located further away from the blades, although there exist confined areas in the proximity of the blades where the lifting line model predictions are still in good agreement with those of the panel code and the SPIV measurements. The latter areas are located at the leading and trailing edges of the blade sections and at the mid-chord upper and lower blade surfaces. As may be noted from Figures 5(c) and 5(f), the region across which errors $\varepsilon_{2,a}$ and $\varepsilon_{3,a}$ are high at $r/R = 0.96$ is larger than for the inboard sections. This is a consequence of the complex 3D flow field induced by the blade tip geometry and the formation of the strong tip vortex in the near wake. In principle, the lifting line representation of the blades is less capable than panel methods in capturing such

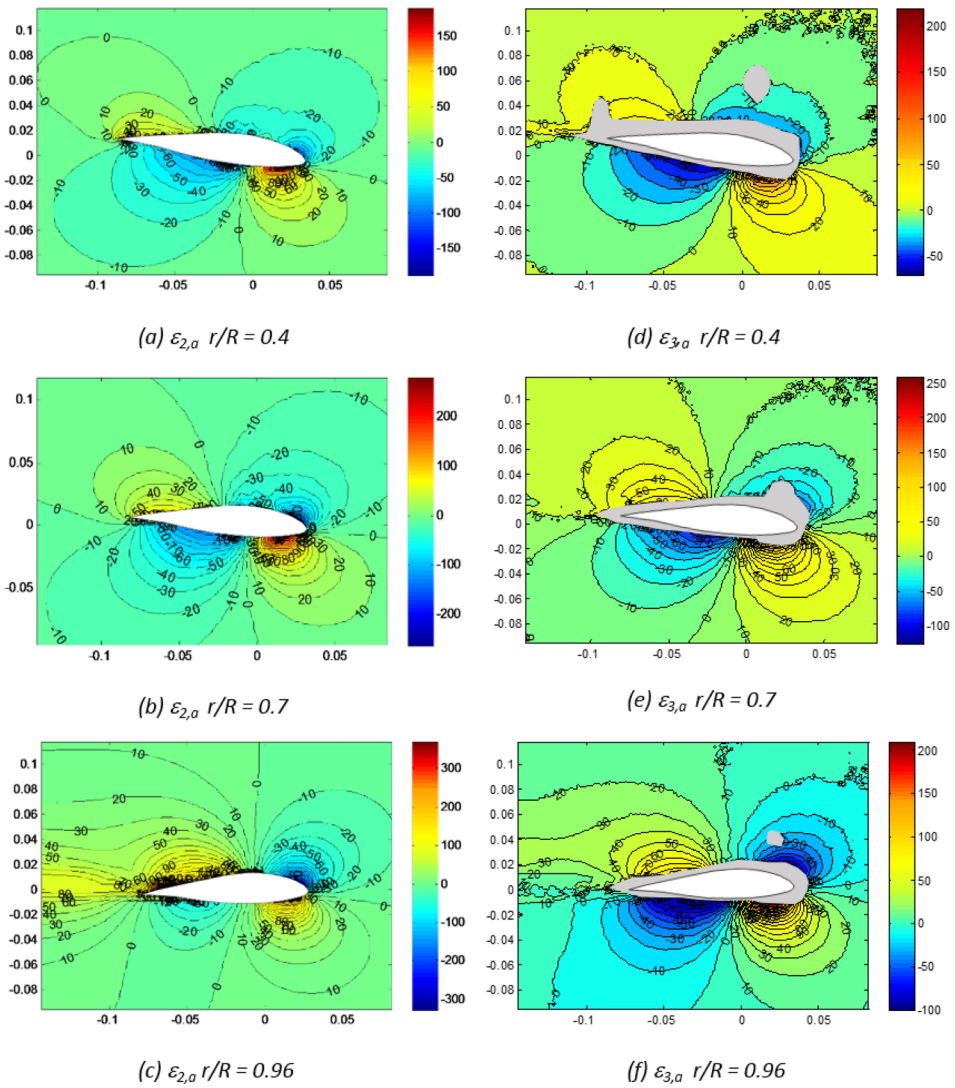

FIG. 5. Contour plots showing distributions for percentage errors $\varepsilon_{2,a}$((a)–(c)) and $\varepsilon_{3,a}$((d)–(f)) around the blades. The x and y coordinates for the flow domain are shown in metres. The bound circulation vortex in the lifting line free wake vortex model is located at the quarter chord location.

three-dimensional effects since the geometry of the blade is modelled in its full 3D detail. Yet, there still exist areas at the outer most regions within the flow domain at $0.96R$ at which the lifting line model prediction errors $\varepsilon_{2,a}$ and $\varepsilon_{3,a}$ are $< 10\%$.

Figure 6 illustrates the contour plots for the lifting line model errors in tangential velocities. The level of agreement between $\varepsilon_{2,t}$ and $\varepsilon_{3,t}$ presented in Figures 6(a)–6(e), respectively, is also reasonably good. Comparing Figures 5 and 6, it can be easily noted that the confined regions around the blades at which the error predictions for the tangential flow are small and do not coincide with those for axial flow. As opposed to axial flow, the confined regions of low $\varepsilon_{2,t}$ and $\varepsilon_{3,t}$ at the upper and lower blade surfaces tend to be located close to the leading and trailing edges rather than in the proximity of the mid-chord. It should be noted that the contour plots presented in Figs. 5 and 6 were generated with the bound vortex of the lifting line model located at the quarter chord location. Different contour plots would be obtained if the location of the bound vortex is altered from the quarter chord location.

Figures 5(d)–5(f) and 6(d)–6(f) indicate masked regions surrounding the airfoil, which resulted from inaccuracies in the SPIV measurements originating from the reflectivity of the

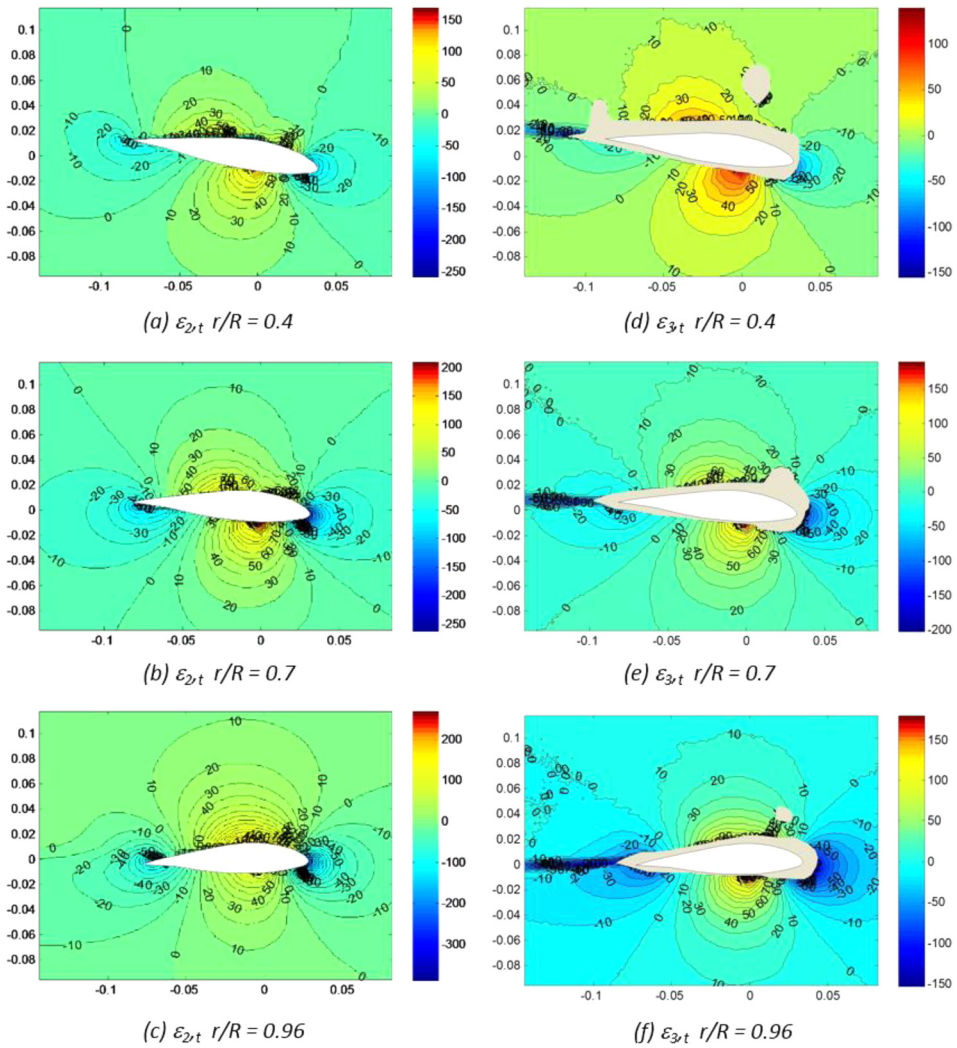

FIG. 6. Contour plots showing distributions for percentage errors $\varepsilon_{2,t}$((a)–(c)) and $\varepsilon_{3,t}$((d)–(f)) around the blades. The x and y coordinates for the flow domains are shown in metres. The bound circulation vortex in the lifting line free wake vortex model is located at the quarter chord location.

blade surfaces. These regions were excluded from the statistical analysis on the error results presented in this paper. A statistical analysis was undertaken to estimate the total respective number of grid points $n_{1,a}$, $n_{2,a}$, and $n_{3,a}$ (and $n_{1,t}$, $n_{2,t}$, *and* $n_{3,t}$) at which the errors $\varepsilon_{1,a}$, $\varepsilon_{2,a}$, and $\varepsilon_{3,a}$ ($\varepsilon_{1,t}$, $\varepsilon_{2,t}$, and $\varepsilon_{3,t}$) were less than different maximum error values. The analysis was repeated for each of the six radial locations (r/R) along the rotor blades. Given that N is the total number of data points within the flow domain, the cumulative probability distributions for the different computed errors listed in Table III could be derived

$$F_a(\varepsilon_{Max,i,a}) = P(\varepsilon_{i,a} \leq \varepsilon_{Max,i,a}) = \frac{n_{i,a}}{N} \quad i = 1, 2, 3, \tag{6a}$$

$$F_t(\varepsilon_{Max,i,t}) = P(\varepsilon_{i,t} \leq \varepsilon_{Max,i,t}) = \frac{n_{i,t}}{N} \quad i = 1, 2, 3. \tag{6b}$$

In the equations above, F_a and F_t denote the cumulative probabilities that the error $\varepsilon_{i,a}$ (and $\varepsilon_{i,t}$) in V_a (and V_t) does not exceed a given maximum error $\varepsilon_{Max,i,a}$ (and $\varepsilon_{Max,i,t}$). F_a and F_t depend on the size of the flow domain, which in this case is 230 mm by 210 mm. The statistically

derived cumulative probability distributions for the axial velocity V_a at r/R equal to 0.4, 0.7, and 0.96 are shown in Figures 7(a)–7(c) while those for the tangential velocity V_t are shown in Figures 7(d)–7(e). It may be observed that F_a and F_t related to the comparison of the panel code to the SPIV measurements (1 PM-PIV) are significantly higher than those comparing the lifting line predictions to the panel code and SPIV results (2 LLM-PM and 3 LLM-PIV). This quantitatively explains the limitations of the LLM in simulating the flow characteristics in the close proximity of the wind turbine blades. The values of F_a and F_t may actually be assumed to be approximately equal to the area out of the domain within which the error is below the given maximum allowable error $\varepsilon_{Max,i,a}$ (and $\varepsilon_{Max,i,t}$). It may be observed from Figure 7 that, in the case of the lifting line model predictions, this area only accounts for to around 25%–30% of the entire domain at a maximum allowable error of 5%. This is far lower than that for the

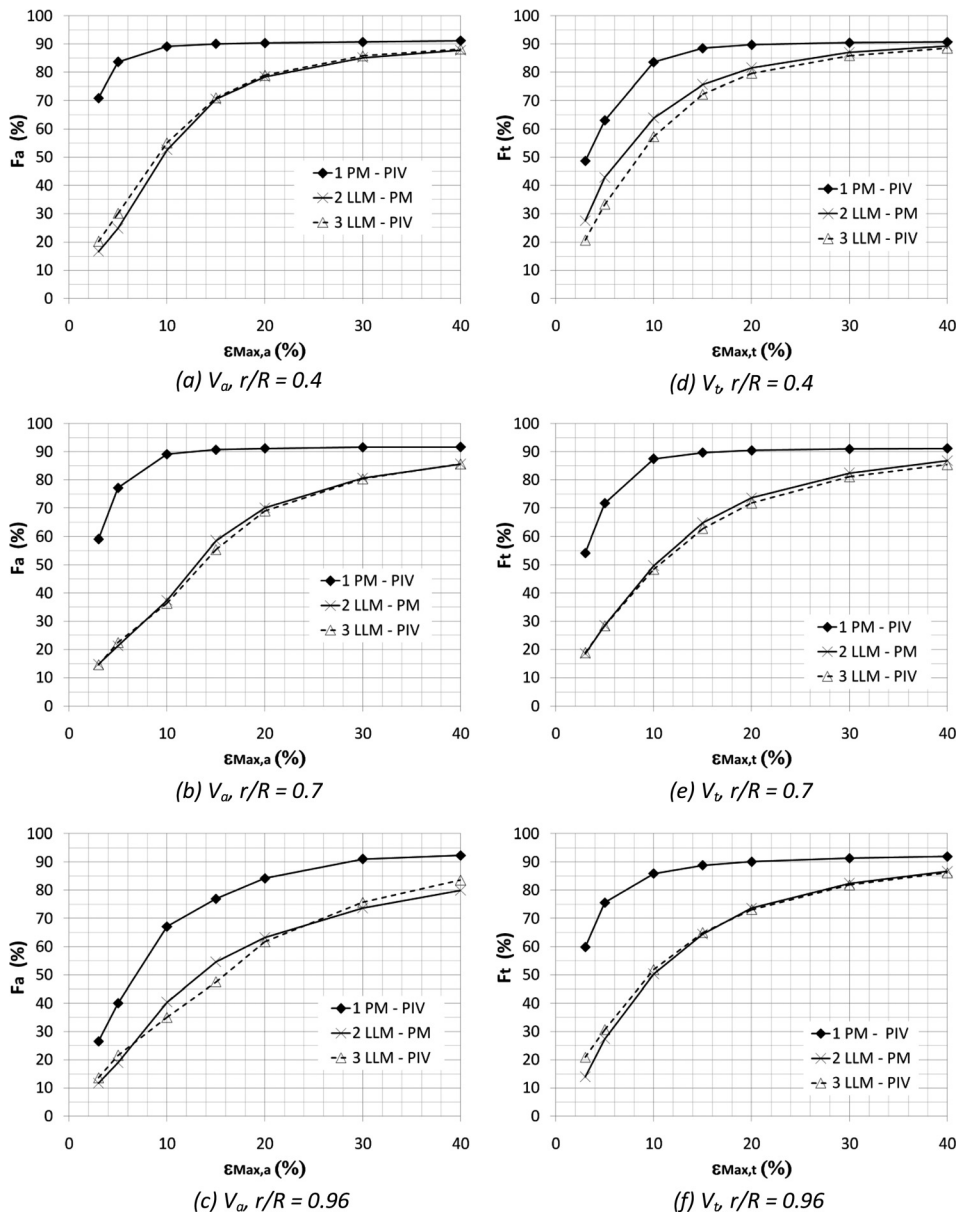

FIG. 7. Cumulative probability distributions for the errors in the predicted axial ((a)–(c)) and tangential ((d)–(f)) velocities around the blades. $\varepsilon_{Max,1}$ – 1 PM – PIV; $\varepsilon_{Max,2}$ – 2 LLM – PM; $\varepsilon_{Max,3}$ – 3 LLM – PIV.

panel vortex model predictions which lies in the range of 45%–85%, depending on radial location. It should be pointed out that the F_a and F_t values for panel code predictions with respect to the SPIV measurements do not reach the 100% limit for $\varepsilon_{1,a}$ and $\varepsilon_{1,t} < 40\%$. This is primarily due to errors incurred by not including a viscous boundary layer model at the blades' surfaces within the panel model. The variations of the error probabilities in the predicted velocity distributions along the different radial locations are presented in Figure 8. The probabilities for maximum allowable error limits of 5%, 10%, and 15% are shown. Figures 8(a)–8(c) show the probabilities for the axial velocities while Figures 8(d)–8(f) are related to the tangential velocity predictions. The F_a value for the panel code (PM) decreases appreciably at the blade tip, indicating increased error predictions when modelling the flow around the blades in the outer radial locations. In the case of the tangential velocities (Figures 8(d)–8(f)), a different trend is observed, with the panel code (PM) F_t values not decreasing towards the tip of the blade. A decrease in F_t is however observed at the inboard location at $r/R = 0.4$. This decrease is more

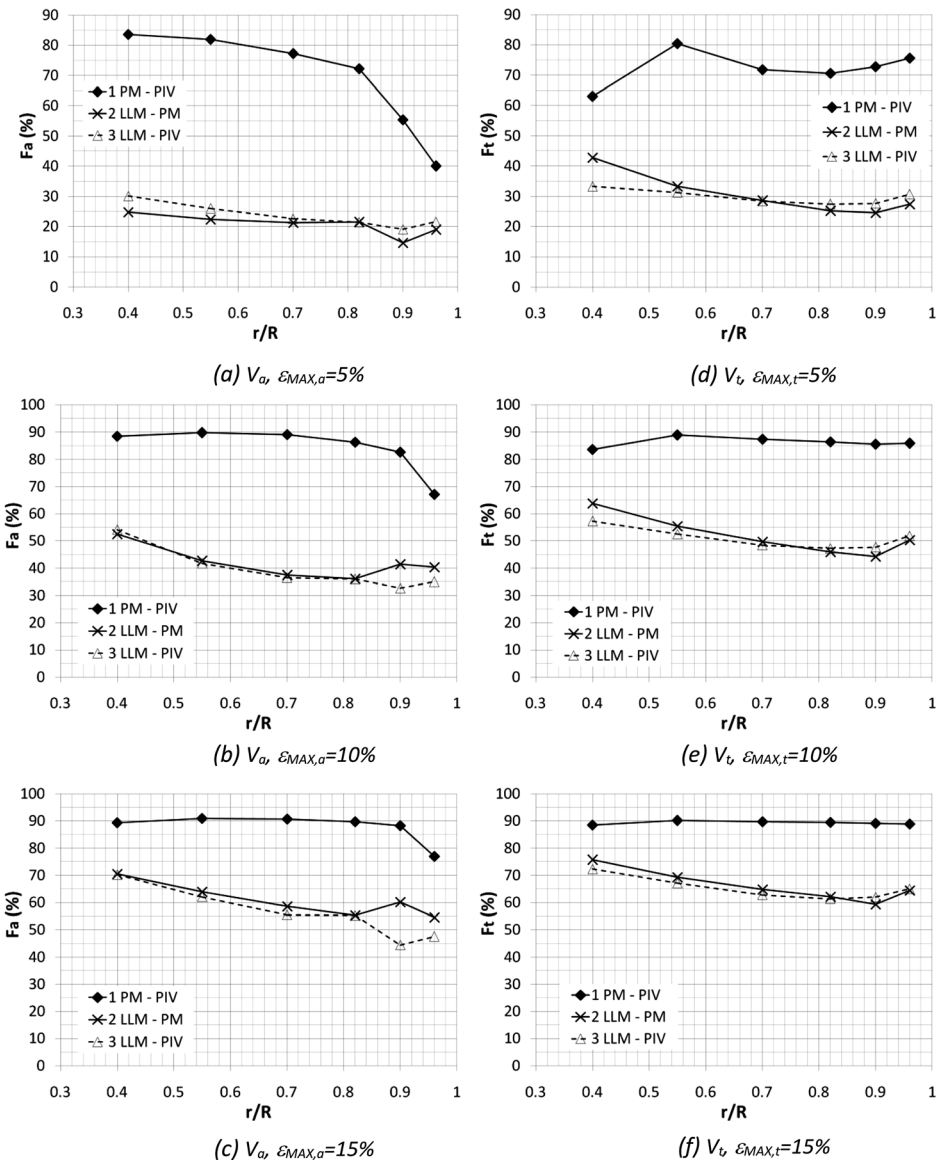

FIG. 8. Variations for the error probabilities for the predicted axial (a) and tangential (b) flow velocity distributions around the blades with radial location (r/R) for a maximum error (ε_{MAX}) of 5%, 10%, and 15%.

prominent for lower values of ε_{Max} (see Figure 8(d)). The probabilities of occurrences within the flow domain for the two independent lifting line model error predictions (*LLM-PM* and *LLM-PIV*) are less sensitive to radial location. Yet these are still significantly lower than those for the panel code (*PM-PIV*). The F_a and F_t values for the lifting line predictions only decrease marginally at the outer blade sections. This shows that, despite the presence of a strong tip vortex and associated complex 3D flows at the blade tip, the lifting line model predictions for the axial and tangential flow fields in this region still have the same order of accuracy as those for the mid-board blade sections. Differences in F_a at the tip region computed for *LLM-PM* and *LLM-PIV* are primarily due to the deficiencies in the panel model in modelling the flow field at this region (see Section III A).

From a direct comparison of Figures 8(a)–8(c) with 8(d)–8(f), it can be noted that the values of F_t for the LLM errors $\varepsilon_{2,t}$ and $\varepsilon_{3,t}$ are slightly larger than the corresponding F_a values. This is being observed for the two independent lifting line model predictions (*LLM-PM* and *LLM-PIV*). It can thus be concluded that the lifting line model is somewhat more reliable, though only marginally, in predicting of tangential flow field than the axial flow one.

Further analysis in the present study involved the computation of the mean ε_m and standard deviation ε_{sd} of the estimated errors $(\varepsilon_{1,a}, \varepsilon_{2,a}, \varepsilon_{3,a}, \varepsilon_{1,t}, \varepsilon_{2,t}$ and $\varepsilon_{3,t})$ over a selected region within the flow domain. The region consisted of two rectangular areas, one located upstream and the other downstream of the blade section (refer to Figure 9). The mean and standard deviation of each error was computed using the following equations:

$$\varepsilon_m = \frac{1}{N}\sum_{i=0}^{N-1} |\varepsilon_i|, \tag{7a}$$

$$\varepsilon_{sd} = \frac{1}{N}\sum_{i=0}^{N-1} (|\varepsilon_i| - \varepsilon_m)^2. \tag{7b}$$

Figures 10 (a) and 10(b) present ε_m and ε_{sd} for the region defined by (t_1,t_2) in Figure 9 equal to (0.04 m, 0.08 m). The values for lifting-line model errors $\varepsilon_{1,a}$ and $\varepsilon_{2,a}$ increase gradually with r/R for the outermost region (refer to Figures 10(a) and 10(b)). The mean and standard deviation values of the lifting line model errors $\varepsilon_{2,t}$ and $\varepsilon_{3,t}$ noted to have the same order of magnitude (Figures 10(c) and 10(d)). Both ε_m and ε_{sd} for the lifting line model remain considerably higher than those of the panel code. Figures 11(a)–11(d) present the mean and standard deviation of the error for three different regions as identified by (t_1,t_2) in Figure 9 such that $t_2 = 0.04$, 0.06,

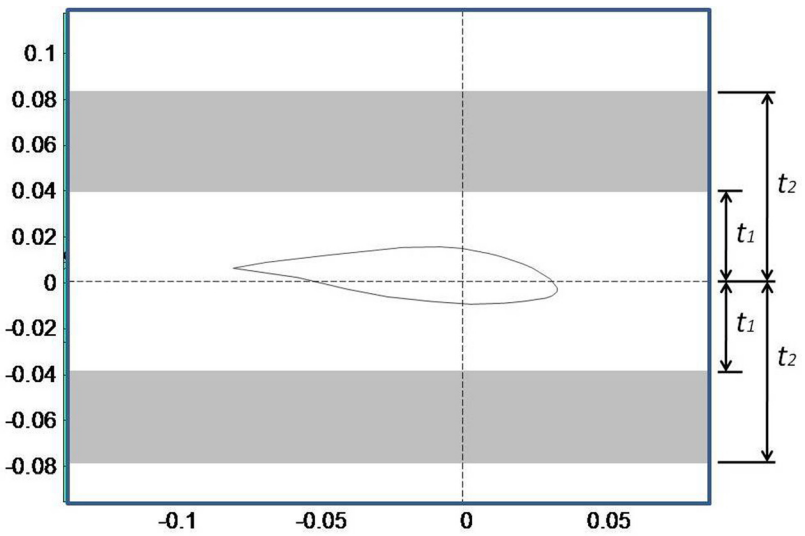

FIG. 9. Regions (shaded) with flow domain around the blades across which ε_m and ε_{sd} were computed.

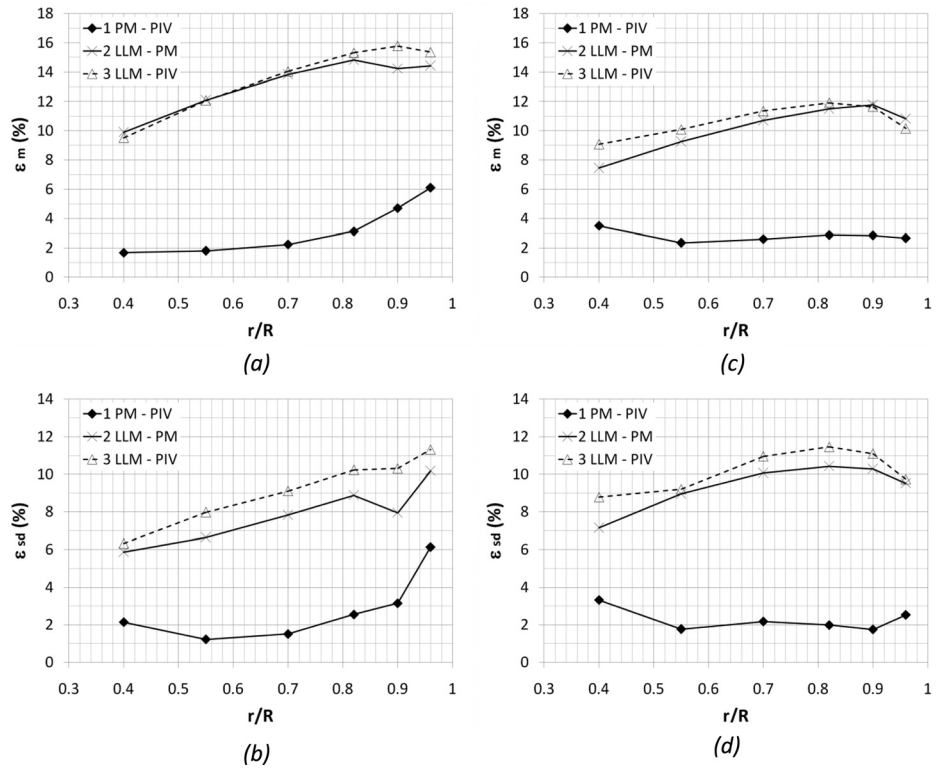

FIG. 10. Variations of the mean (ε_m) and standard deviation (ε_{sd}) of the errors in the predicted axial ((a) and (b)) and tangential ((c) and (d)) flow velocities with radial location (r/R) for region defined by (t_1, t_2) = (0.04, 0.08). ε_1-1 PM-PIV; ε_2-2 LLM-PM; ε_3-3 LLM-PIV.

and 0.08 m while t_2-t_1 is maintained fixed at 0.04 m. The computed error values decrease gradually in a quasi linear manner for the regions further away from the blade.

C. Comparison with 2D flow conditions

The lifting line model is, from a theoretical point of view, a 2D model and relies on the definition of an angle of attack as depicted in Fig. 12 to be able to compute the loads acting on the rotor blades. The applicability of the angle of attack for modelling a rotating wind turbine blade is hence questionable given the flow field in a rotating environment is highly three-dimensional.

In the present study, the errors in the flow field predictions of the lifting line model as compared with panel method ($\varepsilon_{2,a}$ and $\varepsilon_{2,t}$) obtained for the rotating wind turbine blades were compared with those obtained under purely 2D flow conditions for the same angle of attack. The lifting line wind turbine model was used to compute the distributions for the flow velocity (V_r) and angle of attack (α) using the bound circulation from the panel method (Fig. 4). The following steps were then applied for each radial location of the turbine blades:

- Parameters V_r and α (Fig. 12) were used in a 2D panel model for a wing of infinite span having the same chord length equal to that of the turbine blade section under consideration to compute the flow field around the wing section.
- The bound circulation from the 2D panel model calculated in the step above was used to determine the flow field using a 2D lifting line model based on the direct application of the Biot-Savart law.
- The axial and tangential flow fields estimated in the 2D lifting line model were compared with those from the 2D panel model to evaluate the error distributions for the same domain presented in Figs. 5 and 6.

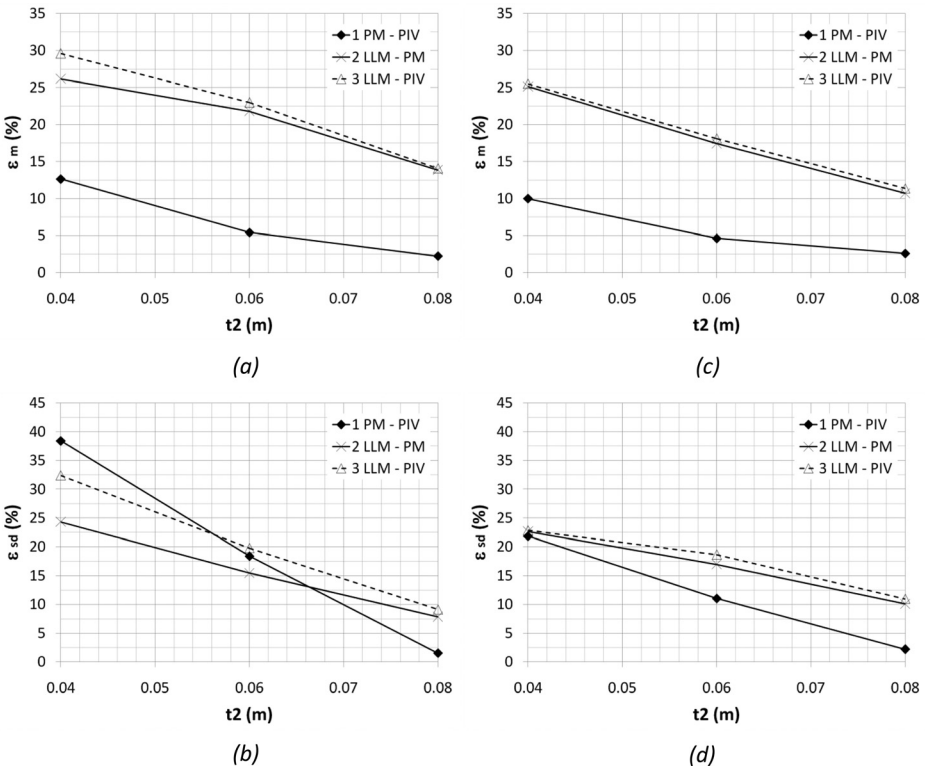

FIG. 11. Variations of the mean (ε_m) and standard deviation (ε_{sd}) of the errors in the predicted axial ((a) and (b)) and tangential ((c) and (d)) flow velocities for (r/R = 70%) with t_2. Values are plotted for (t_1, t_2) = (0.0, 0.04); (0.02, 0.06), and (0.04, 0.08). (t_2-t_1) is maintained fixed equal to 0.04m. ε_1-1 PM-PIV; ε_2-2 LLM-PM; ε_3-3 LLM-PIV.

As observed in Figure 13, the angle of attack at the different blade sections is small and below the static stall angle for the DU96-W180 aerofoil (≈10°). Panel methods are therefore applicable as the flow may be reliably assumed to be fully attached.

Fig. 14 compares the cumulative probability distributions for the axial velocity error ($\varepsilon_{2,a}$) obtained from the lifting line and panel models applied to the rotating wind turbine blades with those obtained from the 2D analysis modelling the infinite wing using the procedure described above. It was revealed that the F_a values from the 2D infinite wing analysis exceeded those obtained for rotating conditions (the latter presented in Figs. 7(a)–7(c) and 8(a)–8(c) (LLM-PM)). This implies that errors incurred in the axial flow field predictions around rotating wind turbine blades when using lifting line models are larger than those incurred when modeling

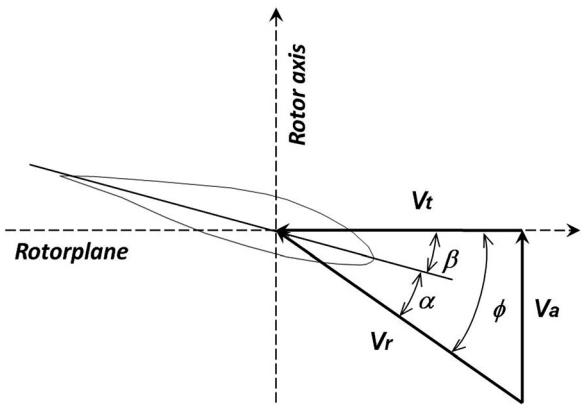

FIG. 12. Blade velocity diagram used in the lifting line model for a wind turbine blade.

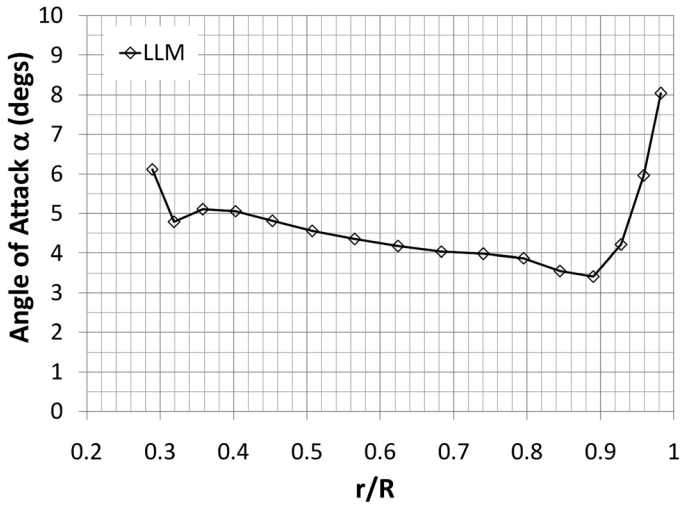

FIG. 13. Angle of attack distribution estimated by lifting line model.

non-rotating wings in 2D flow. Such a trend was observed at all radial locations for both the axial and tangential velocity components, including the mid-board blade locations ($r/R = 0.7$) where the flow is closest to 2D conditions (see Fig. 14(a)). It can therefore be clearly concluded that an analysis solely based on 2D (non-rotating) flow conditions cannot reliably predict the flow field errors in lifting line modelling around rotating wind turbine blades. This results from the influence of trailing circulation shed from wind turbine blades as a consequence of radial variations in bound vorticity. Such radial variations are not present in a 2D flow environment.

D. Derivation of "*No-Go*" Regions for flow field estimations using free-wake lifting line models

This section presents a method for defining "*no-go*" regions when computing the axial and tangential flow field around the wind turbine blades using the lifting line model implemented in free-wake vortex codes. The analysis is restricted to small angles of attack such that the flow around the blade sections is fully attached. The method adopts the ovals developed by Giovanni Domenico Cassini in Ref. 25 to define the boundaries of the "*no-go*" regions. The ovals of Cassini are defined using two focal points, F_1 and F_2, having Cartesian coordinates $(-a, 0)$ and $(a, 0)$, with a point P tracing a locus constrained by the following equation:

$$d_1 d_2 = b^2, \tag{8}$$

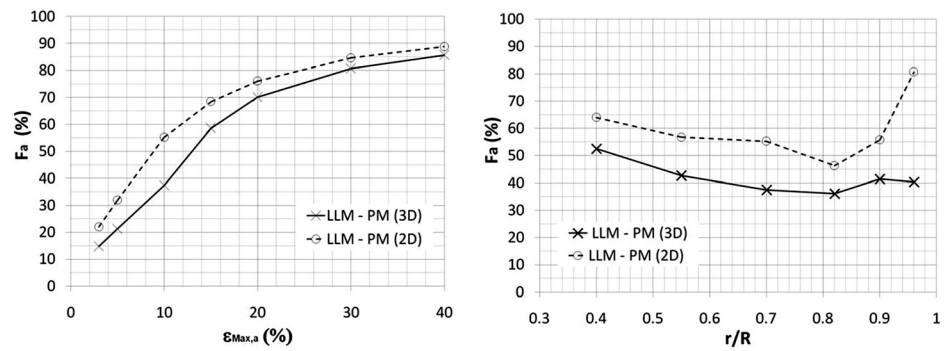

FIG. 14. Probability distributions for the errors in V_a for 3D (rotating) and 2D (infinite wing span) conditions: (a) Cumulative probability distribution at $r/R = 0.7$ and (b) Variation of cumulative probability with radial location for a maximum error (emax) of 10%.

where d_1 and d_2 are the distances PF_1 and PF_2 (Fig. 15(a)). The Cartesian equation defining the Cassini ovals is a quadratic polynomial[22]

$$[(x-a)^2+y^2][(x+a)^2+y^2]=b^4,\ a,b\in\mathcal{R}. \tag{9}$$

The equation above may be expressed in polar coordinates as follows:

$$r=\pm a\sqrt{\cos 2\theta\pm\sqrt{\left(\frac{b}{a}\right)^4-\sin^2 2\theta}},\quad \theta\in[-\theta_0,\theta_0]\text{ and }\quad \theta_o=\frac{1}{2}\sin^{-1}\left[\left(\frac{b}{a}\right)^2\right]. \tag{10}$$

The ratio b/a determines the Cassini shapes (Fig. 15(b)). For $b \gg a$ such that b/a $\rightarrow \infty$, the oval approaches a circle. For $b/a=1$, the curve is a Lemniscate of Bernoulli with the intersection coinciding with the origin O. For $1 < b/a < \sqrt{2}$, the curve is peanut-shaped. The curve splits into two separate ovals for $b/a<1$. *The "no-go"* regions in the present study are derived from the contour plots in Figs. 5 and 6. The boundary for a "*no-go*" region for a given acceptable error ($\varepsilon_{i,a}$ and $\varepsilon_{i,t}$) in the flow fields predicted by the lifting line model is approximated to a Cassini curve with two pairs of focal points with the origin O defined at the blade section mid-chord location ($c/2$). This curve may be plotted by modifying Eq. (10) to

$$r=\pm a\sqrt{\cos 2k(\theta+\varphi)\pm\sqrt{\left(\frac{b}{a}\right)^4-\sin^2 2k(\theta+\varphi)}}, \tag{11}$$

where k is the number of pairs of focal points which in this case is equal to 2. φ is the angle by which the lines joining the two foci of each pair is rotated with respect to the local aerofoil chordline. φ is set to 45° and 0° for defining the *no-go* regions of the axial and tangential flow fields, respectively. The ratio b/a is retained between 1 and $\sqrt{2}$. The resulting defined regions are illustrated in Figs. 16. It can be shown that the maximum and minimum radii, p and q, are equal to $\sqrt{a^2+b^2}$ and $\sqrt{b^2-a^2}$, respectively. Thus, estimates for parameters a and b may be

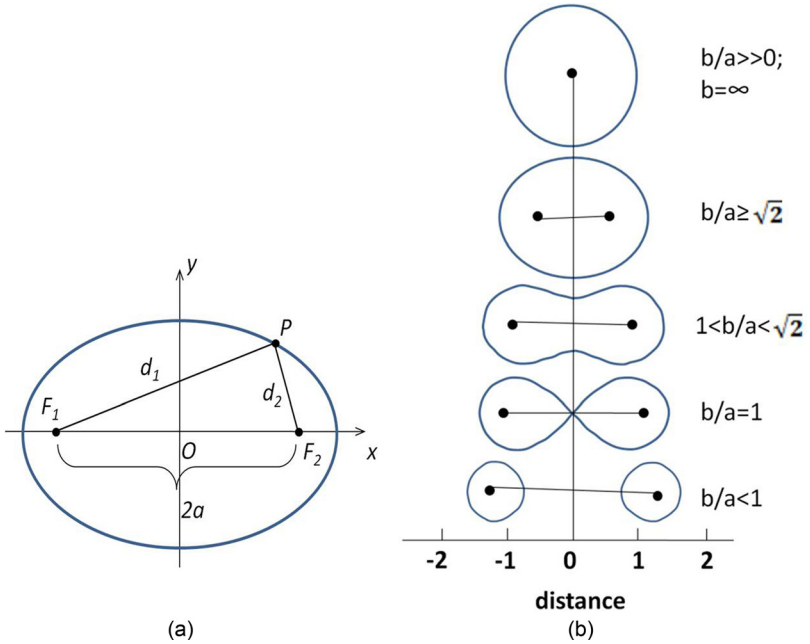

FIG. 15. (a) A Cassini oval with two focal points F_1 *and* F_2 and (b) family of Cassini ovals with two focal points and varying b/a.

reasonably derived from contour error plots similar to Figs. 5 and 6 using the following equations:

$$a = \sqrt{\frac{p^2 - q^2}{2}}; \quad b = \sqrt{\frac{p^2 + q^2}{2}}. \tag{12}$$

Figure 17 shows the parameters defining the *no-go* regions for the axial and tangential flow fields derived from the SPIV measurements. The figure plots the required values of p, q, and a, non-dimensionalised with respect to the local blade chord, to define the boundary of the region within which the errors in the flow field exceed 10%. The values of b/a were kept constant equal to 1.3 and 1.46 for the axial and tangential flow field, respectively. The values are presented only for $0.4 \leq r/R \leq 0.82$. It is noted that the size of the *no-go* region needs to be sized depending on radial location across the blade span. This is related to the bound circulation distribution which increases at the outboard sections for the subject rotor geometry and operating conditions considered in this study (Fig. 4). No values are given in Fig. 17 for the blade tip zone of the blade given that the error distribution cannot be reasonably approximated here by the Cassini curves of Fig. 16. From comparison of Figs. 17(a) and 17(b), it is noted that the size of the *no-go* regions for the tangential flow field may be significantly smaller than those for the axial flow field. This explains why lower errors were noted for the tangential velocity plotted in Fig. 8.

IV. CONCLUSION

This study provides a better understanding of the uncertainties in the lifting line free-wake vortex model predictions for the axial and tangential flow fields around the rotating wind turbine blades. The quantitative assessment was based on two independent sources: numerical predictions from a 3D inviscid panel method and SPIV measurements. Although there were discrepancies in the bound circulation and flow fields derived from these two sources, both indicated similar trends about the error distributions in flow field predictions from lifting line models. The level of uncertainty in the lifting line method was found to be significant. However there still exist confined areas in the flow domain close to a wind turbine blade at which the lifting line method can still predict both the axial and tangential flow velocities with a reasonable degree of accuracy. Such confined areas for the axial flow velocity do not coincide with those for the tangential flow fields. Furthermore, the study revealed that, although highly

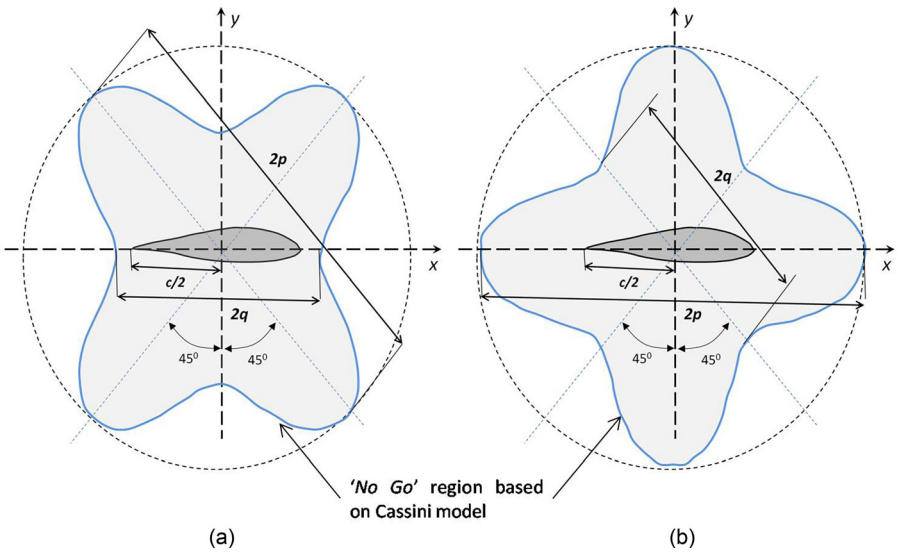

FIG. 16. Definition of *no-go* region using Cassini curves for (a) axial flow field and (b) tangential flow field.

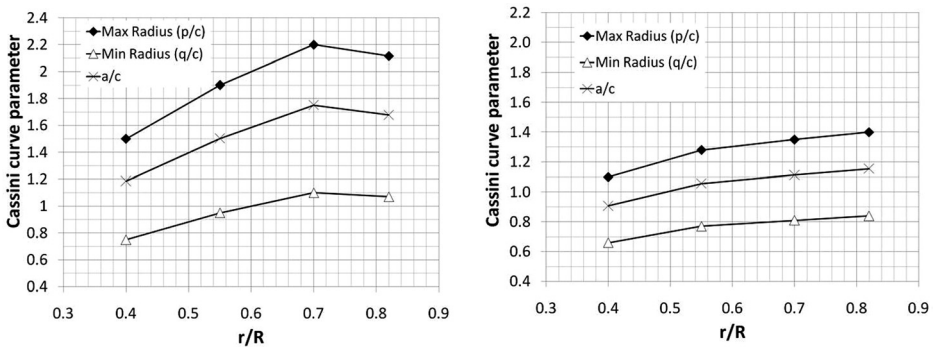

FIG. 17. Parameters defining *no-go* regions around the blade for lifting line model predictions for the axial (a) and tangential (b) flow fields not to exceed an error ($\varepsilon_{3,a}$ and $\varepsilon_{3,t}$) of 10% when compared to SPIV measurements.

3D phenomena induced by the strong tip vorticity are present at the blade tip region, the accuracy in the lifting line predictions for the axial and tangential flow fields here is still in the same order of magnitude as that for the mid-board region. The accuracy with which the lifting line method predicts the tangential component was also found to be marginally higher that for the axial component.

The study has shown that the level of uncertainty in the flow field predictions from lifting line models for a rotating blade is larger than those obtained for equivalent 2D (non-rotating) conditions with a wing of infinite span. This trend was observed at all radial locations, including the mid-board regions of the blade. Consequently, lifting line models for 2D non-rotating flows cannot reliably estimate error distributions in lifting line model predictions for 3D rotating blades.

A new method based on Cassini's oval theory was presented for defining *no-go* regions around the wind turbine blades where lifting line model predictions for the flow field are unreliable. The method was applied to the two bladed rotor; however, this had to be limited to $0.4 \leq r/R \leq 0.82$ as it was found not to be applicable at the blade tip region. The lack of applicability at the outboard region ($r/R > 0.82$) is mainly due to the 3D flows effects induced by the strong tip vorticity which are more dominant in rotors having a low aspect ratio and a relatively large chord length at the tip, as in the case of the rotor investigated in this study. The degree of applicability of the Cassini oval theory is hence expected to extend beyond $r/R = 0.82$ for large scale wind turbine blades which have a larger aspect ratio and a gradually decreasing chord length at the tip. This is however subject to more detailed investigations with full-scale rotors.

The definitions of *no-go* regions may serve as a useful guideline for determining the extent to which lifting line free-wake vortex models can reliably estimate the flow field around the rotating wind turbine blades. One useful application of the proposed approach using the Cassini ovals method could possibly be in hybrid CFD/free-wake vortex methods whereby Navier Stokes (NS) solvers are used to model the detailed flow field close to the rotor blades while the free-wake vortex filament method simulates the rotor wake development. The Cassini based *no-go* regions may be utilised to determine flow domain geometries for the mesh-based NS solution which may be optimised in the coupling process to the free-wake vortex solver to minimise computational cost while still retaining sufficient accuracy in predicting aerodynamic loads and flow fields.

[1]H. Snel, "Review of aerodynamics of wind turbines," Wind Energy **6**, 203–211 (2003).
[2]L. J. Vermeer, J. N. SØrensen, and A. Crespo, "Wind turbine wake aerodynamics," Prog. Aerospace Sci. **39**, 467–510 (2003).
[3]M. Hansen, J. SØrensen, S. Voutsinas, N. SØrensen, and H. Madsen, "State of the art in wind turbine aerodynamics and aeroelasticity," Prog. Aerospace Sci. **42**(4), 285–330 (2006).
[4]B. Sanderse, *Aerodynamics of Wind Turbine Wakes* (National Energy Research Foundation, 2009), ECN-E-09-016.
[5]M. Hansen and H. Madsen, "Review paper on wind turbine aerodynamics," J. Fluids Eng. **133**(11), 114001 (2011).
[6]J. G. Leishman, M. J. Bhagwat, and A. Bagai, "Free-vortex filament methods for the analysis of helicopter rotor wakes," J. Aircraft **39**(5), 759–775 (2002).

[7]A. van Garrel, *Development of a Wind Turbine Aerodynamics Simulation Module* (National Energy Research Foundation, 2003), ECN-C-03-079.
[8]T. Sebastian and M. A. Lackner, "Development of a Free-wake vortex method code for offshore floating wind turbines," Renewable Energy **46**, 269–275 (2012).
[9]S. G. Voutsinas, M. A. Belessis, and S. Huberson, "Dynamic inflow effects and vortex particle methods," in *Proceedings from the European Wind Energy Conference, Lubeck-Travemunde, Germany*, 1993.
[10]D. J. Lee and S. U. Na, "Numerical simulations of wake structures generated by rotating blades using a time marching free vortex blob method," Eur. J. Mech. **18**, 147 (1999).
[11]J. Katz and A. Plotkin, *Low-Speed Aerodynamics: From Wing Theory to Panel Methods*, 2nd ed. (Cambridge University Press, 2001).
[12]A. van Garrel, *Development of a Wind Turbine Rotor Flow Panel Method* (Energy Research Centre of the Netherlands, 2011), ECN-E-11-071, see www.ecn.nl.
[13]S. P. Breton., F. N. Coton, and G. Moe, "A study on rotational effects and different stall delay models using a prescribed wake vortex scheme and NREL phase VI experiment data," Wind Energy **11**(5), 459–482 (2008).
[14]J. G. Holierhoek, J. B. de Vaal, A. H. van Zuiljen, and H. Bijl, "Comparing different dynamic stall models," Wind Energy **16**(1), 139–158 (2013).
[15]V. Del Campo, D. Ragni, D. Micallef, B. Akay, F. J. Diez, and C. S. Ferreira, "3D load calculation on a horizontal axis wind turbine using SPIV," Wind Energy **17**, 1645–1657 (2013).
[16]D. Micallef, "3D flows near a HAWT rotor: A dissection of blade and wake contributions," Ph.D. thesis (TU Delft and University of Malta, 2012).
[17]J. Westerweel, "Digital particle image velocimetry: Theory and application," Ph.D. thesis (TU Delft, 1993).
[18]M. Raffel, C. E. Willert, and J. Kompenhans, *Particle Image Velocimetry: A Practicalguide* (Springer Verlag, 1998).
[19]M. Ramasamy and J. G. Leishman, "A generalized model for transitional blade tip vortices," J. Am. Helicopter Soc. **51**(1), 92–103 (2006).
[20]M. Ramasamy and J. G. Leishman, "A Reynolds number-based blade tip vortex model," J. Am. Helicopter Soc. **52**(3), 214–223 (2007).
[21]C. S. Ferreira, "The near wake of the VAWT: 2D and 3D views of the VAWT aerodynamics," Ph.D. thesis (Technische Universiteit Delft, The Netherlands, 2009).
[22]D. Micallef, G. J. W. van Bussel, C. S. Ferreira, and T. Sant, "An investigation of radial velocities for a HAWT in axial and yawed flow," Wind Energy **16**, 529–544 (2013).
[23]T. Sant, G. A. M. van Kuik, and G. J. W. van Bussel, "estimating the angle of attack from blade pressure measurements on the nrel phase VI rotor using a free-wake vortex model: Axial conditions," Wind Energy **9**(6), 549–577 (2006).
[24]D. Micallef, C. S. Ferreira, T. Sant, and G. J. W. van Bussel, "Experimental and numerical investigation of tip vortex generation and evolution on horizontal axis wind turbines," Wind Energy (published online 2015).
[25]M. Karatas, "A multi foci closed curve: Cassini oval, its properties and applications," Dogus Univ. J. **14**(2), 231–248 (2013), ISSN: 1302-6739, e-ISSN: 1308-6979.